3D harmonic modeling of eddy currents in segmented conducting structures

Abstract

Purpose —- The purpose of this paper is to describe a semi-analytical modeling technique to predict eddy currents in 3-dimensional conducting structures with finite dimensions. Using the developed method, power losses and parasitic forces that result from eddy current distributions can be computed.

Design/methodology/approach — In conducting regions, the Fourier-based solutions are developed to include a spatially dependent conductivity in the expressions of electromagnetic quantities. To validate the method, it is applied to an electromagnetic configuration and the results are compared to finite element results.

Findings —- The method shows good agreement with the finite element method for a large range of frequencies. The convergence of the presented model is analyzed.

Research limitations/implications —- Due to the Fourier series basis of the solution, the results depend on the considered number of harmonics. When conducting structures are small with respect to the spatial period, the number of harmonics have to be relatively large.

Practical implications —- Due to the general form of the solutions, the technique can be applied to a wide range of electromagnetic configurations to predict e.g. eddy current losses in magnets, or wireless energy transfer systems. By adaptation of the conductivity function in conducting regions, eddy current distributions in structures containing holes or slit patterns can be obtained.

Originality/value —- With the presented technique, eddy currents in conducting structures of finite dimensions can be modeled. The semi-analytical model is for a relatively low number of harmonics computationally faster than 3D finite element methods. The method has been validated and shown to be computationally accurate.

Keywords Modelling, Magnetic fields, Semi-analytical, Eddy currents, Fourier
Paper type Research paper

3D Harmonic Modeling of Eddy Currents in Segmented Conducting Structures

C.H.H.M. Custers, J.W. Jansen, M.C. van Beurden and E.A. Lomonova
Department of Electrical Engineering, Eindhoven University of Technology, Eindhoven, The Netherlands

I. Introduction

In applications where time-varying magnetic fields are present, eddy currents are induced in conducting materials. High-frequent magnetic fields, which are present in high-speed machines or in PWM inverter fed machines (Yamazaki and Abe, 2009), lead to induced currents and thereby significant power losses. In electrical machines, eddy currents typically cause losses in the magnets (Wu *et al.*, 2012; Nair *et al.*, 2017; Benlamine *et al.*, 2015; Lee *et al.*, 2013), conducting sleeves (Hannon *et al.*, 2017; Shah and Lee, 2006; Jumayev *et al.*, 2016) or other conducting parts (Rovers *et al.*, 2011; Paul and Bird, 2013; Fireteanu *et al.*, 2002). Also in wireless power transfer systems, (Kim *et al.*, 2016; Xiao *et al.*, 2017; Kim *et al.*, 2015), eddy currents significantly influence the performance. For high-precision (nanometer accurate) positioning devices, used in e.g. the lithographic industry, where also high accelerations are demanded, the parasitic forces due to eddy currents can be a limiting factor for performance and position accuracy. As a solution, the eddy currents are often reduced by means of segmentation of the conducting parts (Takahashi *et al.*, 2009; Ede *et al.*, 2007; Mirzaei *et al.*, 2010). With the technique developed in this paper, eddy current distributions in, for example, the slitted cooling plates and permanent magnets of a moving-magnet planar motor and the related parasitic force- and torque components can be analyzed, (Custers *et al.*, 2017*b*).

To investigate the spatial distribution and harmonic content of induced currents in structures that are segmented in multiple directions, a two-dimensional (2D) model does often not suffice and a three-dimensional model (3D) is needed. Furthermore, to correctly calculate eddy current distributions induced by high-frequent fields, the reaction field of the eddy currents has to be included in the formulation of the model. The computation of eddy current distributions in complex structures puts enormous demands on the 3D finite element method (FEM) (Nakano *et al.*, 2013), with respect to memory and computation time. In the FEM, the degrees of freedom are for this reason often reduced using edge element based approximations instead of node based approximations in regions where eddy currents are considered (Bossavit, 1988). An accurate (semi)-analytical model can be a relatively fast and more memory efficient alternative to the FEM.

Semi-analytical models that can calculate 3D static magnetic fields and developed forces in electromagnetic devices have, among others, been described in (Jansen *et al.*, 2014). By analytically implementing the static magnetic Maxwell equations, eddy current distributions can be obtained from the magnetic field (Ede *et al.*, 2007; Zhu *et al.*, 2015). In this case, however, the reaction field of the eddy currents is not taken into account and only resistance-limited eddy currents can be calculated. To include the reaction field of eddy currents, the quasi-static Maxwell equations have to be implemented, which is possible with the harmonic (or Fourier-based) model (Dwivedi *et al.*, 2016; Meessen *et al.*, 2012; Paul and Bird, 2013). To solve the quasi-static Maxwell equations often a first or second order vector potential is introduced, as described in (Theodoulidis *et al.*, 1995; Jumayev *et al.*, 2016; Hannon *et al.*, 2017). In these researches, however, the assumption was made that the conductor is infinitely long (not segmented).

To consider the shape of segmented conducting parts in the harmonic model, the spatial dependence of the conductivity of the geometry under consideration has to be included in the solutions. Several researches have successfully implemented a spatially varying magnetic permeability in the solutions of the magnetic field in either 2D or 3D (Custers *et al.*, 2016) models. For a 2D harmonic problem, a spatially varying electric conductivity was included to model eddy currents in segmented conductors, as described in (Custers *et al.*, 2017*a*). To extend this model and to obtain eddy current distributions in segmented parts of a 3D model in the Cartesian coordinate system, a formulation is applied where the Maxwell equations are directly solved using a coupled magnetic and electric field formulation. Formulations using a vector potential as used in (Custers *et al.*, 2017*a*) or a second-order vector potential (Theodoulidis *et al.*, 1995; Jumayev *et al.*, 2016; Hannon *et al.*, 2017) or a combination of the vector potential with a scalar potential (Biro and Preis, 1989), have been investigated by the authors. With the harmonic model, which has Fourier based solutions, these formulations were not implementable or gave inaccurate results.

In this paper, a formulation is presented to include a spatially varying electric conductivity in the solutions of electromagnetic field quantities of a 3D harmonic model. The model is defined in the Cartesian coordinate system and is assumed periodic in two directions and the basis of the solutions to the fields is therefore a double Fourier series. In regions that do not contain a conductor, the standard Fourier-based solutions, derived from a magnetic potential are described. Hereafter, the expressions for the magnetic field and the induced current density in a region containing conducting segments are given. For this type

Corresponding author: c.h.h.m.custers@tue.nl

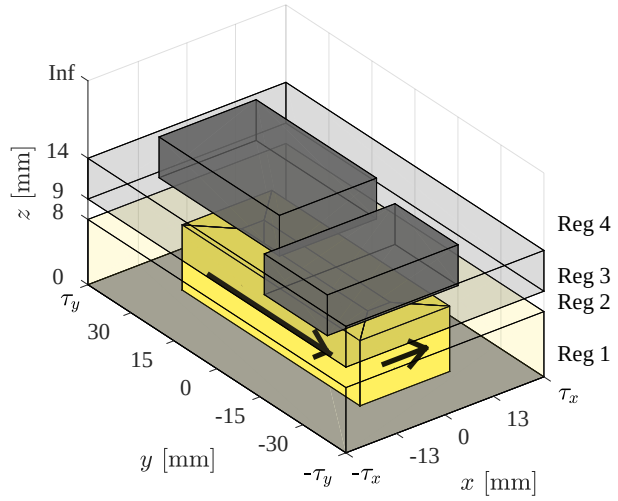

Fig. 1. Three-dimensional geometric model of two conducting plates (gray) placed above a time-varying current carrying coil (yellow).

of region, the tangential components of the electric and magnetic field are used to derive the fields. Furthermore, the spatial dependency of the conductivity is taken into account. The boundary conditions to connect all regions are explained and the final solutions in each region are obtained. The method is then applied to a periodic electromagnetic configuration, containing a coil and two finite pieces of conducting material. The convergence of the obtained solution is analyzed and the results are compared to finite element analysis to verify the model.

II. Magnetic Field Modeling in Non-Conducting Regions

The expressions for the magnetic field quantities are derived in this section by starting from Maxwell's equations. Furthermore, a geometry is described that contains several types of regions and that is used to validate the developed model. Because a general solution for each region is described, any geometry consisting of these types of regions can be constructed and modeled.

A. Model assumptions

The coordinate system of the geometry that is modeled is the Cartesian coordinate system. The model is periodic in both the x- and y-directions, while in the z-direction it is divided in regions. The types of regions that are considered are source, air and conducting regions. In a source region, either a magnetization (magnet) or current density (coil) is imposed, which creates a magnetic field. It is assumed that the imposed current density is homogeneously distributed inside the coil volume and that no currents are induced in the coil. A magnet can be conducting, however for simplification of the equations it is either considered as a non-conducting magnet or a conducting non-magnetic material. In a conducting region, some kind of conducting material is present, but it only has to partially span the periodic region. This means that a part of the conducting region can have a conductivity value equal to zero. Furthermore, it is assumed that no sources (magnetization or imposed current density) are present in a conducting region. No source or conducting material is present in an air region. All material properties in the model are considered to be linear, homogeneous and isotropic and throughout each region the permeability is assumed constant as a function of position. The incorporation of a spatially dependent permeability of a region in the Fourier-based model is described in (Custers *et al.*, 2016).

B. Geometric model

In Fig. 1, a 3D electromagnetic configuration, which will be used to validate the semi-analytical method, is shown. In this model, two conducting plates are placed above a coil. The current flowing through the coil is time varying, which causes induced currents in the conducting plates above. The current direction in the coil is indicated by the arrows. The two plates are not connected to each other, so no induced current can flow from one plate to the other. In the z-direction, a number of regions is created as depicted in Fig. 1. Region 2 and 4 contain only air, and Region 3 contains air and the two rectangular plates of conducting material. The current carrying coil is located in Region 1. The bottom surface of Region 1 is assumed to be infinitely permeable.

C. Description of the general solution

It is assumed that all fields are quasi-static, so the displacement current, $\frac{\partial \vec{D}}{\partial t}$, is neglected. For an $e^{j\omega t}$ time dependence of the fields and sources, the time derivative can be denoted by $j\omega$. The relevant Maxwell equations for the problem are

$$\nabla \times \vec{E} = -j\omega \vec{B}, \tag{1}$$

$$\nabla \times \vec{H} = \vec{J}, \tag{2}$$

$$\nabla \cdot \vec{B} = 0, \tag{3}$$

where $\vec{E}$ is the electric field strength, $\vec{H}$ the magnetic field strength, $\vec{B}$ the magnetic flux density, and $\vec{J}$ is the electric current density.

In the non-conducting regions, only static magnetic fields have to be considered and a potential is introduced to calculate the magnetic field quantities. In a region containing only air or magnets, the scalar potential ψ is used. The magnetic field strength $\vec{H}$ is obtained from ψ through

$$\vec{H} = -\nabla \psi. \tag{4}$$

The constitutive relation is given by

$$\vec{B} = \mu_0 \left(\vec{H} + \vec{M} \right), \tag{5}$$

where μ_0 is the permeability of vacuum and $\vec{M}$ is the magnetization. By combining (3), (4), and (5) and by assuming constant permeability, the Poisson equation for the magnetic scalar potential is obtained

$$\nabla^2 \psi = \frac{1}{\mu_r} \nabla \cdot \frac{\vec{B}_{rem}}{\mu_0}, \tag{6}$$

where μ_r is the relative permeability and $\vec{B}_{rem}$ is the remanent flux density of a magnet. For an air region, the right-hand side of (6) is equal to zero.

In a region containing current carrying coils (no magnets) the vector potential $\vec{A}$ is used, defined as

$$\vec{B} = \nabla \times \vec{A}. \tag{7}$$

By substituting (7) in (2) the Poisson equation for the vector potential is obtained, i.e.

$$\nabla^2 \vec{A} = -\mu_0 \mu_r \vec{J}^{imp}, \tag{8}$$

where $\vec{J}^{imp}$ is the imposed current density. A coil is placed in the model in such way that no current is flowing in the z-direction. The vector potential will then only have non-zero x- and y- components, and A_z is equal to zero. For conducting regions, where currents can be induced, a different formulation is used, which is described in Section III.

The solution to (6) and (8) is found via the method of separation of variables. The electromagnetic field solutions and other position dependent quantities, can be written with a double (truncated) Fourier series as basis because of periodicity in the x- and y-directions

$$f(x,y) = \sum_{m=-M/2}^{M/2} \sum_{n=-N/2}^{N/2} \mathbf{f} \left\{ \left(n + \frac{N}{2} \right) + \left(m + \frac{M}{2} \right) (N+1) \right\} \; e^{j(k_{x,n} x + k_{y,m} y)}. \tag{9}$$

In (9), n and m are the harmonic numbers and $k_{x,n}$ and $k_{y,m}$ are the spatial frequencies in the x- and y-directions, respectively. The spatial frequencies are given by

$$k_{x,n} = \frac{n\pi}{\tau_x}, \tag{10}$$

$$k_{y,m} = \frac{m\pi}{\tau_y}, \tag{11}$$

where τ_x and τ_y are half the periodic widths in the x- and y-directions, respectively. The Fourier series have to be truncated for implementation purposes. This means that a finite number of harmonics is used, equal to $N+1$ and $M+1$ in the x- and y-directions, respectively. The column vector $\mathbf{f}$, which index is zero-based, contains the Fourier coefficients of the double series. The index $\left(n + \frac{N}{2}\right) + \left(m + \frac{M}{2}\right)(N+1)$ selects the correct entry for each harmonic pair.

From (6), the expression for the coefficients of the scalar potential in matrix form is obtained

$$\boldsymbol{\psi} = j\boldsymbol{\Lambda} \left(\boldsymbol{\Theta}^{+}(\boldsymbol{\lambda}, z) \; \mathbf{c}^{+} - \boldsymbol{\Theta}^{-}(\boldsymbol{\lambda}, z) \; \mathbf{c}^{-} + \mathbf{p}_{\psi} \right), \tag{12}$$

where $\mathbf{p}_{\psi}$ is the particular solution and $\mathbf{c}^{+}$ and $\mathbf{c}^{-}$ are unknowns per harmonic pair n, m collected in column vectors of size 1 x $(N+1)(M+1)$. The unknowns are obtained by applying boundary conditions between the different types of regions, which is described in Section IV. The z-dependent solution consists of two parts, denoted by $\boldsymbol{\Theta}^{+}$ and $\boldsymbol{\Theta}^{-}$, which are exponential

functions growing or decaying as a function of z. The matrices $\mathbf{\Theta}^+$, $\mathbf{\Theta}^-$ and $\mathbf{\Lambda}$ of size $(N+1)(M+1)$ x $(N+1)(M+1)$ are given by

$$\mathbf{\Theta}^+(\boldsymbol{\lambda}, z) = \text{diag}\left(e^{\boldsymbol{\lambda}(z-z_T)}\right), \tag{13}$$

$$\mathbf{\Theta}^-(\boldsymbol{\lambda}, z) = \text{diag}\left(e^{-\boldsymbol{\lambda}(z-z_B)}\right), \tag{14}$$

$$\mathbf{\Lambda} = \text{diag}\left(\boldsymbol{\lambda}\right). \tag{15}$$

The mathematical notation 'diag()' in (13), (14) and (15) denotes a diagonal matrix, formed from the entries of the input vector on the diagonal. For scaling purposes, a constant is subtracted from z in the exponent. The constants z_T and z_B are respectively the maximum and minimum z-coordinate of a certain region. In Fig. 1, z_T of Region 3 is equal to 14 mm and z_B is equal to 9 mm. The subtraction of the constants ensures that the modulus of the exponential function is always between 0 and 1, which improves the conditioning of the matrix that is formed after applying the boundary conditions between regions (see Section V). The vector $\boldsymbol{\lambda}$ contains the propagation constants of the solution. For a region described by either the scalar or vector potential (Regions 1, 2 and 4 in Fig. 1), $\boldsymbol{\lambda}$ is given by

$$\boldsymbol{\lambda} = \sqrt{\mathbf{k_x}^2 + \mathbf{k_y}^2}, \tag{16}$$

which is to be understood element-wise and where the vectors $\mathbf{k_x}$ and $\mathbf{k_y}$ contain the spatial frequencies. The frequencies are collected in the vectors in such a way that the index of the coefficients $\left(n+\frac{N}{2}\right)+\left(m+\frac{M}{2}\right)(N+1)$ in (9) selects the correct entry

$$\mathbf{k_x} = \begin{bmatrix} \begin{bmatrix} k_{x,-N/2} \\ \vdots \\ k_{x,0} \\ \vdots \\ k_{x,N/2} \end{bmatrix} \\ \begin{bmatrix} k_{x,-N/2} \\ \vdots \\ k_{x,0} \\ \vdots \\ k_{x,N/2} \end{bmatrix} \\ \vdots \end{bmatrix} \begin{matrix} \left.\begin{matrix} \\ \\ \\ \\ \\ \end{matrix}\right\} \text{Size: } N+1 \\ \\ \\ \\ \\ \end{matrix} \quad \mathbf{k_y} = \begin{bmatrix} \begin{bmatrix} k_{y,-M/2} \\ \vdots \\ k_{y,-M/2} \\ \vdots \\ k_{y,-M/2} \end{bmatrix} \\ \begin{bmatrix} k_{y,-M/2+1} \\ \vdots \\ k_{y,-M/2+1} \\ \vdots \\ k_{y,-M/2+1} \end{bmatrix} \\ \vdots \end{bmatrix} \begin{matrix} \left.\begin{matrix} \\ \\ \\ \\ \\ \end{matrix}\right\} \text{Size: } N+1 \\ \\ \\ \\ \\ \end{matrix}. \tag{17}$$

From the vectors $\mathbf{k_x}$, $\mathbf{k_y}$, diagonal matrices can be constructed

$$\mathbf{K_x} = \text{diag}(\mathbf{k_x}), \tag{18}$$

$$\mathbf{K_y} = \text{diag}(\mathbf{k_y}), \tag{19}$$

and these will be used in the continuation of the paper.

From (8), the coefficients of the components of the vector potential can be calculated. The z-component of the vector potential is assumed to be zero as explained in (Smeets *et al.*, 2013), and the other components are then equal to

$$\mathbf{a_x} = \mathbf{K_y}\left(\mathbf{\Theta}^+(\boldsymbol{\lambda}, z)\ \mathbf{c}^+ + \mathbf{\Theta}^-(\boldsymbol{\lambda}, z)\ \mathbf{c}^-\right) + \mathbf{p}_{a_x}, \tag{20}$$

$$\mathbf{a_y} = -\mathbf{K_x}\left(\mathbf{\Theta}^+(\boldsymbol{\lambda}, z)\ \mathbf{c}^+ + \mathbf{\Theta}^-(\boldsymbol{\lambda}, z)\ \mathbf{c}^-\right) + \mathbf{p}_{a_y}, \tag{21}$$

$$\mathbf{a_z} = 0, \tag{22}$$

where $\mathbf{p}_{a_x}$ and $\mathbf{p}_{a_y}$ are again particular solutions. Expressions for the coefficients of the components of $\vec{B}$ and $\vec{H}$ can be calculated by applying (4), (5) and (7) to the expression for the magnetic scalar or vector potential. These expressions are given in the Appendix.

When the conductivity of a region is varying as a function of position (Region 3 in Fig. 1), the derivation of the propagation constants is more elaborate. The propagation constants and an accompanying eigenvector have to be derived, with the spatial dependence of the conductivity incorporated. The calculation of this propagation information for conducting regions is described in Section III.

The particular solutions, $\mathbf{p}_\psi$, $\mathbf{p}_{a_x}$ and $\mathbf{p}_{a_y}$, depend on the source terms in (6) and (8), i.e. the magnetization or imposed current density terms. For a source region described by the scalar potential, the particular solution $\mathbf{p}_\psi$ can be determined from (6) and is equal to

$$\mathbf{p}_\psi = -j\frac{1}{\mu_r}\left(\mathbf{K_x}^2 + \mathbf{K_y}^2\right)^{-1}\left(\mathbf{K_x}\mathbf{m_x} + \mathbf{K_y}\mathbf{m_y}\right), \tag{23}$$

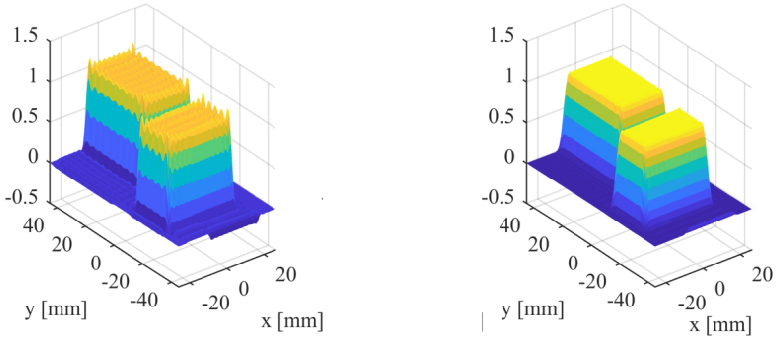

Fig. 2. Truncated Fourier series description of the conductivity in Region 3. a) Fourier description without Lanczos sigma factor multiplication. b) Fourier description with Lanczos sigma factor multiplication.

where $\mathbf{m_x}$ and $\mathbf{m_y}$ are the Fourier coefficients describing the spatially dependent magnetization in the x- and y-direction respectively. The particular solutions $\mathbf{p}_{a_x}$ and $\mathbf{p}_{a_y}$ for a source region with the vector potential formulation are given by

$$\mathbf{p}_{a_x} = \mu_0\mu_r \left(\mathbf{K_x}^2 + \mathbf{K_y}^2\right)^{-1} \mathbf{j}_{\boldsymbol{x}}^{\boldsymbol{imp}}, \tag{24}$$

$$\mathbf{p}_{a_y} = \mu_0\mu_r \left(\mathbf{K_x}^2 + \mathbf{K_y}^2\right)^{-1} \mathbf{j}_{\boldsymbol{y}}^{\boldsymbol{imp}}, \tag{25}$$

where $\mathbf{j}_{\boldsymbol{x}}^{\boldsymbol{imp}}$ and $\mathbf{j}_{\boldsymbol{y}}^{\boldsymbol{imp}}$ are the Fourier coefficients describing the imposed current density in the x- and y-direction respectively. The Fourier coefficients of the magnetization and imposed current density can be computed based on the geometrical shape and physical parameters of the source. For non-square shapes of the source, such as the corners of the coil segments in Fig. 1, the Fourier coefficients are calculated using the method presented in (Pluk *et al.*, 2015).

III. Magnetic Field Modeling for Regions with a Spatially Varying Conductivity

In (Custers *et al.*, 2015), a technique is presented in which the spatial dependency of the conductivity is incorporated in a 2D Fourier model. To model the eddy currents in conducting regions, the vector potential formulation was utilized. However, to correctly model regions with a spatially varying conductivity in the 3D model, the vector potential formulation does not suffice. In this section the magnetic field and induced current expressions for a segmented 3D conducting region are derived using the tangential components of the $\vec{H}$ and $\vec{E}$ field.

A. Tangential $\vec{E}$ and $\vec{H}$ field components

To find the expressions for $\vec{H}$ and $\vec{B}$ for a region with a spatially varying conductivity, no potential is introduced. Instead, the tangential components of $\vec{E}$ and $\vec{H}$ are used. The induced current density $\vec{J}^{ind}$ can be derived from the electric field

$$\vec{J}^{ind} = \sigma(x,y)\vec{E}. \tag{26}$$

The conductivity $\sigma(x,y)$ in (26) is the position dependent conductivity in the region, which is described by a double Fourier series. Because the conductivity is zero in the air outside the plates, the Fourier coefficients $\boldsymbol{\sigma}$ are expressed as

$$\boldsymbol{\sigma} = \sigma_{pl}\boldsymbol{\eta}, \tag{27}$$

where σ_{pl} is the value of the conductivity of the material of the plates and $\boldsymbol{\eta}$ is the vector containing the Fourier coefficients of the function describing the conductivity as one inside the plates and zero outside. A Fourier truncated version of this function is shown in Fig. 2a.

To obtain a stable final solution for a large number of harmonics, the Fourier series of the source terms ($\vec{J}^{imp}$) and of the function describing the conductivity are multiplied by the Lanczos sigma factor (Hamming, 1986)

$$f(x,y) = \sum_{m=-M/2}^{M/2} \sum_{n=-N/2}^{N/2} \operatorname{sinc}\frac{|n|}{N/2+1} \operatorname{sinc}\frac{|m|}{M/2+1} \mathbf{f}\left\{\left(n+\frac{N}{2}\right) + \left(m+\frac{M}{2}\right)(N+1)\right\} e^{j(k_{x,n}x + k_{y,m}y)}. \tag{28}$$

The multiplication with the Lanczos sigma factor reduces the Gibss effect (Hamming, 1986) present in a Fourier expanded function as shown in Fig. 2.

Equations (1) and (2) can be written separately for each Cartesian component of $\vec{E}$ and $\vec{H}$. Substituting the z-components

$$E_z = -\sigma^{-1}(x,y)\left(\partial_x H_y - \partial_y H_x\right), \tag{29}$$

$$H_z = \left(j\omega\mu_0\right)^{-1}\left(\partial_x E_y - \partial_y E_x\right), \tag{30}$$

into the remaining four equations gives

$$\partial_z E_x = \quad j\omega\mu_0 H_y - \partial_x \left(\sigma^{-1}(x,y)\left(\partial_x H_y - \partial_y H_x\right)\right), \tag{31}$$

$$\partial_z E_y = -j\omega\mu_0 H_x - \partial_y \left(\sigma^{-1}(x,y)\left(\partial_x H_y - \partial_y H_x\right)\right), \tag{32}$$

$$\partial_z H_x = -\sigma(x,y) E_y + (j\omega\mu_0)^{-1}\partial_x \left(\left(\partial_x E_y - \partial_y E_x\right)\right), \tag{33}$$

$$\partial_z H_y = \quad \sigma(x,y) E_x + (j\omega\mu_0)^{-1}\partial_y \left(\left(\partial_x E_y - \partial_y E_x\right)\right). \tag{34}$$

In (31)-(34) several multiplications of $\sigma(x,y)$ (or its inverse) with one of the field components appears. Because both terms of these multiplications are double Fourier series, in the spectral domain, a 2D discrete convolution of the Fourier coefficients should be performed. For this purpose, the coefficients of $\sigma(x,y)$, $\boldsymbol{\eta}$, are written in a block-Toeplitz matrix (Jayaraman *et al.*, 2011, p. 110-122) denoted by $\boldsymbol{\mathcal{P}}$. From this point onward, matrix equations are used because they simplify the derivation of the solution. Expressing (31)-(34) in two matrix equations results in

$$\frac{\partial}{\partial z}\begin{bmatrix}\mathbf{e_x}\\ \mathbf{e_y}\end{bmatrix} = \begin{bmatrix}-\mathbf{K_x}\boldsymbol{\mathcal{P}}^{-1}\mathbf{K_y} & j\omega\mu_0\mathbf{I} + \mathbf{K_x}\boldsymbol{\mathcal{P}}^{-1}\mathbf{K_x}\\ -j\omega\mu_0\mathbf{I} - \mathbf{K_y}\boldsymbol{\mathcal{P}}^{-1}\mathbf{K_y} & \mathbf{K_y}\boldsymbol{\mathcal{P}}^{-1}\mathbf{K_x}\end{bmatrix}\begin{bmatrix}\mathbf{h_x}\\ \mathbf{h_y}\end{bmatrix} = \mathbf{F}\begin{bmatrix}\mathbf{h_x}\\ \mathbf{h_y}\end{bmatrix}, \tag{35}$$

$$\frac{\partial}{\partial z}\begin{bmatrix}\mathbf{h_x}\\ \mathbf{h_y}\end{bmatrix} = \begin{bmatrix}(j\omega\mu_0)^{-1}\mathbf{K_x}\mathbf{K_y} & -\boldsymbol{\mathcal{P}} - (j\omega\mu_0)^{-1}\mathbf{K_x}^2\\ \boldsymbol{\mathcal{P}} + (j\omega\mu_0)^{-1}\mathbf{K_y}^2 & -(j\omega\mu_0)^{-1}\mathbf{K_y}\mathbf{K_x}\end{bmatrix}\begin{bmatrix}\mathbf{e_x}\\ \mathbf{e_y}\end{bmatrix} = \mathbf{G}\begin{bmatrix}\mathbf{e_x}\\ \mathbf{e_y}\end{bmatrix}, \tag{36}$$

where, $\mathbf{e_x}$, $\mathbf{e_y}$, $\mathbf{h_x}$ and $\mathbf{h_y}$ are the vectors containing the Fourier coefficients of E_x, E_y, H_x, and H_y, respectively.

If the conductivity would have been constant throughout the region, the block-Toeplitz matrix $\boldsymbol{\mathcal{P}}$ could have been replaced by σ_{pl} in (35) and (36). One could observe that in this case, because of diagonal sub-matrices throughout the matrix, the solution to the coefficient of $\frac{\partial}{\partial z}\mathbf{e_x}$ with index i would only depend on $\mathbf{h_x}\{i\}$ and $\mathbf{h_y}\{i\}$. The same analysis is valid for all components of $\vec{E}$ and $\vec{H}$. However, the incorporation of the spatial dependency of the conductivity in the form of the block-Toeplitz (non-diagonal) matrix causes $\frac{\partial}{\partial z}\mathbf{e_x}\{i\}$ to depend on all coefficients of $\mathbf{h_x}$ and $\mathbf{h_y}$. The spatial harmonics are now coupled, in contrast to the problem where the conducting part spans the entire periodic region, and all spatial harmonics will be decoupled and independent from each other.

It should be noted that the inverse of the matrix describing the spatially dependent conductivity $\boldsymbol{\mathcal{P}}$ is mathematically not correct because it is zero at certain locations (see Fig. 2). The block-Toeplitz matrix $\boldsymbol{\mathcal{P}}^{-1}$ is therefore not obtained by inversion of $\boldsymbol{\mathcal{P}}$ but is formed from the coefficients of $\frac{1}{\sigma_{pl}}\boldsymbol{\eta}$. The use of a complex permittivity in the formulation, which is also non-zero outside the conducting material, was investigated but did not show a different result or increased stability.

By substituting (35) in (36), it is obtained that

$$\frac{\partial^2}{\partial z^2}\begin{bmatrix}\mathbf{h_x}\\ \mathbf{h_y}\end{bmatrix} = \mathbf{GF}\begin{bmatrix}\mathbf{h_x}\\ \mathbf{h_y}\end{bmatrix}. \tag{37}$$

To obtain the vector with propagation constants for the region with varying conductivity, an eigenvalue decomposition is performed on the matrix $\mathbf{GF}$, i.e.

$$\begin{bmatrix}\mathbf{Q_x}\\ \mathbf{Q_y}\end{bmatrix}\ \boldsymbol{\Lambda}^2\ \begin{bmatrix}\mathbf{Q_x}\\ \mathbf{Q_y}\end{bmatrix}^{-1} = \mathbf{GF}, \tag{38}$$

where $\boldsymbol{\Lambda}$ is a matrix containing the vector $\boldsymbol{\lambda}$ with propagation constants on the diagonal and $\mathbf{Q_x}$ and $\mathbf{Q_y}$ are matrices containing the eigenvectors belonging to each eigenvalue. The matrix $\boldsymbol{\Lambda}$ is squared in (38), because in (37) a double derivative to z is performed. The vector of propagation constants for a region with conducting materials has double the size of the vector in a non-conducting region. This is due to the coupling of spatial harmonics. Also the size of the vectors containing the unknowns will double as a result. With $\boldsymbol{\lambda}$ obtained, the solution for $\mathbf{h_x}$ and $\mathbf{h_y}$ is found to be

$$\mathbf{h_x} = \mathbf{Q_x}\left(\boldsymbol{\Theta}^+(\boldsymbol{\lambda},z)\ \mathbf{c}^+ - \boldsymbol{\Theta}^-(\boldsymbol{\lambda},z)\ \mathbf{c}^-\right), \tag{39}$$

$$\mathbf{h_y} = \mathbf{Q_y}\left(\boldsymbol{\Theta}^+(\boldsymbol{\lambda},z)\ \mathbf{c}^+ - \boldsymbol{\Theta}^-(\boldsymbol{\lambda},z)\ \mathbf{c}^-\right). \tag{40}$$

The expression for the coefficients of the z-component of the magnetic field strength, $\mathbf{h_z}$, is calculated from (3) and is equal to

$$\mathbf{h_z} = -j\left(\mathbf{K_x}\mathbf{Q_x} + \mathbf{K_y}\mathbf{Q_y}\right)\boldsymbol{\Lambda}^{-1}\ \left(\boldsymbol{\Theta}^+(\boldsymbol{\lambda},z)\ \mathbf{c}^+ + \boldsymbol{\Theta}^-(\boldsymbol{\lambda},z)\ \mathbf{c}^-\right) \tag{41}$$

The expressions for the components of the magnetic flux density can be calculated from (5). The solution for the induced current density components, $\mathbf{j_x^{ind}}$, $\mathbf{j_y^{ind}}$ and $\mathbf{j_z^{ind}}$ are determined from (1) and (26), i.e.

$$\mathbf{j_x^{ind}} = \ \mathbf{Q_y}\ \boldsymbol{\Lambda}\left(\boldsymbol{\Theta}^+(\boldsymbol{\lambda},z)\ \mathbf{c}^+ + \boldsymbol{\Theta}^-(\boldsymbol{\lambda},z)\ \mathbf{c}^-\right) - j\mathbf{K_y}\mathbf{h_z}, \tag{42}$$

$$\mathbf{j_y^{ind}} = -\mathbf{Q_x}\ \boldsymbol{\Lambda}\left(\boldsymbol{\Theta}^+(\boldsymbol{\lambda},z)\ \mathbf{c}^+ + \boldsymbol{\Theta}^-(\boldsymbol{\lambda},z)\ \mathbf{c}^-\right) + j\mathbf{K_x}\mathbf{h_z}, \tag{43}$$

$$\mathbf{j_z^{ind}} = j\mathbf{K_y}\mathbf{h_x} - j\mathbf{K_x}\mathbf{h_y}. \tag{44}$$

IV. Boundary Conditions

By applying boundary conditions between the various regions, the values of the unknowns $(\mathbf{c}^+, \mathbf{c}^-)$ for each region can be obtained.

The continuity boundary condition forces continuation of the tangential $\vec{H}$ components and the normal $\vec{B}$ component on a certain boundary. On the boundary at z-position, z_{cont}, the continuous boundary condition between, e.g. Regions I and II, is given by

$$H_{x,I}|_{z=z_{cont}} = H_{x,II}|_{z=z_{cont}}, \tag{45}$$
$$H_{y,I}|_{z=z_{cont}} = H_{y,II}|_{z=z_{cont}}, \tag{46}$$
$$B_{z,I}|_{z=z_{cont}} = B_{z,II}|_{z=z_{cont}}. \tag{47}$$

The boundary condition in this form is applied between a conducting region (solutions presented in Section III) and a non-conducting region (solutions presented in Section II). However, if the continuous boundary condition is applied between two non-conducting regions, an over-determined problem is constructed. The number of equations is in this case larger than the number of unknowns. Therefore, instead of the continuity of H_x and H_y the continuity of the scalar potential is forced on this boundary, as described in (Smeets *et al.*, 2013), i.e.

$$\psi_I|_{z=z_{cont}} = \psi_{II}|_{z=z_{cont}}. \tag{48}$$

For a source region with the vector potential formulation (e.g. Region 1 in Fig. 1) an expression for the scalar potential has to be obtained to be able to apply the boundary condition of (48). This expression can be obtained from (4) as

$$\psi = -\int H_x \; dx = -\int H_y \; dy. \tag{49}$$

The second type of boundary condition that is used is the Dirichlet boundary condition. It forces any component of the magnetic field strength, magnetic flux density, or scalar potential to a specific value at a certain z-coordinate. On a boundary with infinite permeability (e.g. the bottom and top surface in Fig. 1) the tangential components of the magnetic field strength are forced to zero. For example, if the surface of Region I is infinitely permeable at height z_{Dir} the boundary condition is given by

$$H_{x,I}|_{z=z_{Dir}} = 0, \tag{50}$$
$$H_{y,I}|_{z=z_{Dir}} = 0. \tag{51}$$

In case of a non-conducting region, (50) and (51) are also combined into one boundary condition for the scalar potential, to avoid an over-determined problem, i.e.

$$\psi_I|_{z=z_{Dir}} = 0. \tag{52}$$

Furthermore, the Dirichlet condition can be applied to force the field components of a region to zero if the region extends to infinity

$$\vec{H}|_{z=\pm\infty} = \vec{B}|_{z=\pm\infty} = \vec{0}. \tag{53}$$

This boundary condition implies that one of the two unknowns ($\mathbf{c}^+$ or $\mathbf{c}^-$) in the solution is set to zero.

V. Calculation of Coefficients

By applying the boundary conditions between regions, a system of linear equations is constructed. The coefficients for each region are obtained by solving the system of equations,

$$\mathbf{E_{tot}} \; \mathbf{c} = \mathbf{y}, \tag{54}$$

where,

$$\mathbf{E_{tot}} = \begin{bmatrix} \boldsymbol{\Theta}^+{}_1(\boldsymbol{\lambda}_1, z_1) & -\boldsymbol{\Theta}^-{}_1(\boldsymbol{\lambda}_1, z_1) & \mathbf{0} & \cdots \\ \boldsymbol{\Theta}^+{}_1(\boldsymbol{\lambda}_1, z_2) & -\boldsymbol{\Theta}^-{}_1(\boldsymbol{\lambda}_1, z_2) & -\boldsymbol{\Theta}^+{}_2(\boldsymbol{\lambda}_2, z_2) & \cdots \\ \boldsymbol{\Lambda}_1\boldsymbol{\Theta}^+{}_1(\boldsymbol{\lambda}_1, z_2) & \boldsymbol{\Lambda}_1\boldsymbol{\Theta}^-{}_1(\boldsymbol{\lambda}_1, z_2) & -\boldsymbol{\Lambda}_2\boldsymbol{\Theta}^+{}_2(\boldsymbol{\lambda}_2, z_2) & \cdots \\ \mathbf{0} & \mathbf{0} & \boldsymbol{\Theta}^+{}_2(\boldsymbol{\lambda}_2, z_2) & \cdots \\ \vdots & \vdots & \vdots & \ddots \end{bmatrix}, \quad \mathbf{c} = \begin{bmatrix} \mathbf{c}^+{}_1 \\ \mathbf{c}^-{}_1 \\ \mathbf{c}^+{}_2 \\ \vdots \\ \mathbf{c}^-{}_I \end{bmatrix}, \quad \mathbf{y} = \begin{bmatrix} \mathbf{y}_1 \\ \mathbf{y}_2 - \mathbf{y}_1 \\ . \\ \vdots \\ \mathbf{y}_I \end{bmatrix}, \tag{55}$$

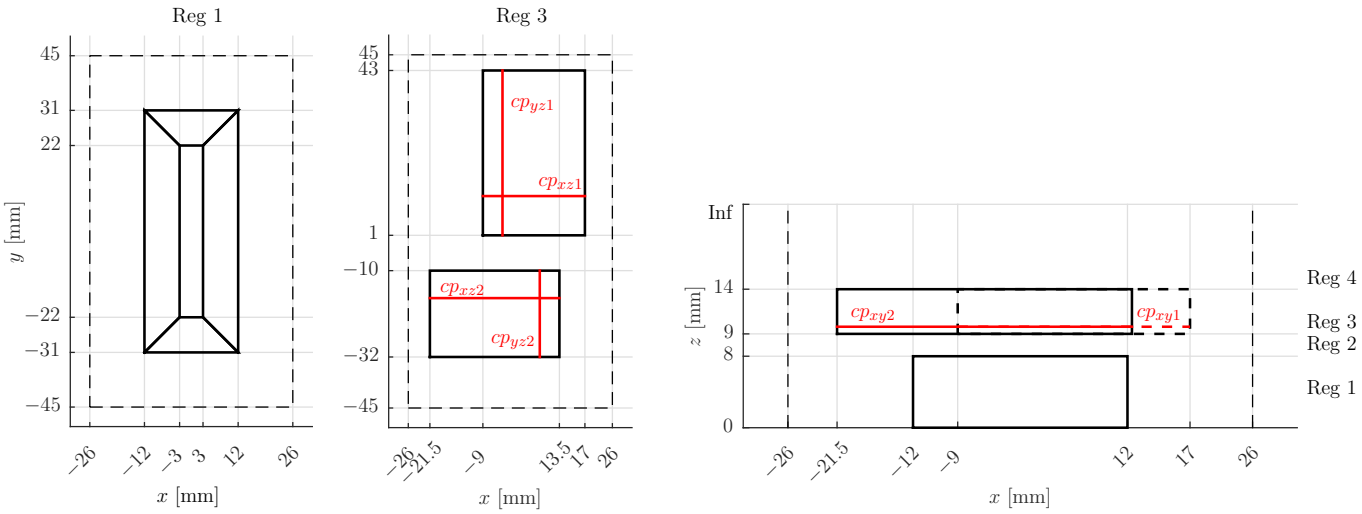

Fig. 3. Dimensions of the coil and plates in the modeled geometry: a) xy-view, b) xz-view.

and where $\mathbf{y}$ are the coefficients of the particular solutions and any other additional source-related terms, which are known in advance. Because each region has its own expressions and unknowns, a subscript denoting the region is added to all variables and sub-matrices in the matrix and arrays of (55). The number of regions depends on the geometry under consideration, so the total number of regions is denoted by I. The height z_i is the height of boundary between Region i and Region $i+1$. The sub-matrix $\mathbf{0}$ contains only zeros.

VI. Force and Power Calculation

To calculate the force exerted between objects, the Maxwell stress tensor T_{ij} (Furlani, 2001) is used. It is applied on the surfaces of a box, located in air, enclosing the object on which the force $\vec{F}$ is considered

$$\vec{F} = \oint_S \langle T_{ij} \rangle \cdot \hat{\mathbf{n}} \, ds. \tag{56}$$

The time-averaged stress tensor for complex magnetic fields is given by

$$\langle T_{ij} \rangle = \frac{1}{2} \mathrm{Re} \left\{ \frac{1}{\mu_0} B_i B_j^* \right\} - \frac{1}{4} \frac{1}{\mu_0} \delta_{ij} \left(B_i B_i^* \right), \tag{57}$$

where δ_{ij} is the Kronecker delta. On a surface parallel to the xy-plane where $\hat{z}$ is the vector normal to the plane, using (56) and (57) the force is calculated as

$$F_x = \int_{-\tau_y}^{\tau_y} \int_{-\tau_x}^{\tau_x} \frac{1}{2} \mathrm{Re} \left\{ \frac{1}{\mu_0} B_x B_z^* \right\} \, dx \, dy, \tag{58}$$

$$F_y = \int_{-\tau_y}^{\tau_y} \int_{-\tau_x}^{\tau_x} \frac{1}{2} \mathrm{Re} \left\{ \frac{1}{\mu_0} B_y B_z^* \right\} \, dx \, dy, \tag{59}$$

$$F_z = \int_{-\tau_y}^{\tau_y} \int_{-\tau_x}^{\tau_x} \frac{1}{4} \frac{1}{\mu_0} B_z B_z^* \, dx \, dy. \tag{60}$$

In the same way, the force can be calculated for surfaces parallel to the xz- or yz-plane. For the electromagnetic configuration shown in Fig. 1, a xy-surface integral in the center of the airgap between the coil and the conducting parts suffices to calculate the force components.

To calculate the power loss in a conducting segment, a volume integration over the volume of the conducting segment is performed, i.e.

$$P_{loss} = \frac{1}{\sigma_{pl}} \int_V \vec{J}^{ind} \cdot \left(\vec{J}^{ind} \right)^* dv. \tag{61}$$

The surface and volume integrals are performed numerically. It has been made sure that the spatial discretization step in the z-direction is less than one fourth of the skin depth at a certain frequency.

TABLE I
MODEL PARAMETERS

Description	Value	Unit
Peak current	1.3	A
Number of turns in the coil	100	-
Conductivity of the plates in Region 3	25	MS/m

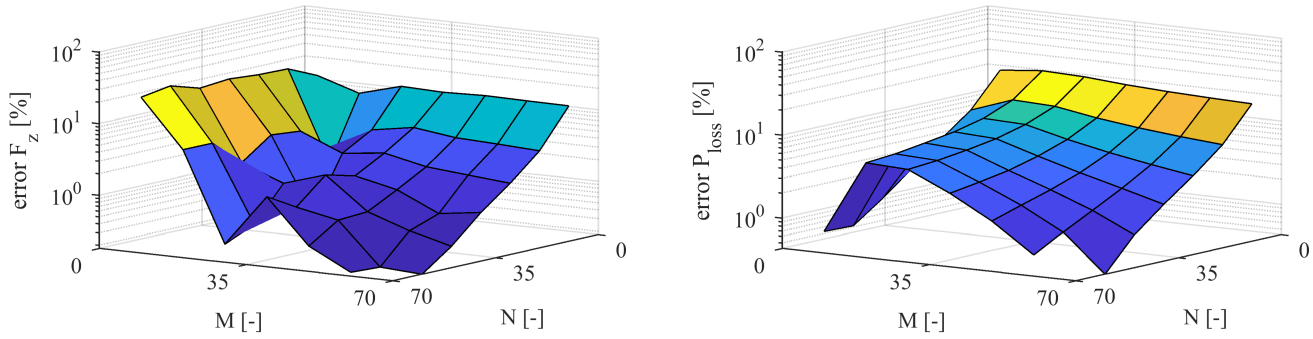

(a) (b)

Fig. 4. Convergence plots as a function of the number of harmonics at a frequency of 100 Hz. The relative error with respect to the result at $N = M = 70$ is calculated for each harmonic pair: a) convergence of the force in the z-direction, b) convergence of the power loss (in both conducting segments).

VII. RESULTS

To analyze the performance of the developed semi-analytical method (in figures denoted by ANA), results are compared to the finite element method (FEM). First, the convergence of the developed model is tested on the geometric model of Fig. 1. The frequency at which eddy currents can be analyzed in the finite element model depends on the mesh size. To obtain reliable results, at least 3 second-order mesh elements per skin depth are used. With the memory available for the mesh, the maximum frequency at which eddy currents can be accurately calculated is equal to 10 kHz. Details on the employed FEM software and implemented mesh are given in Section VII-B.

A. Convergence of the solution

The method developed in the preceding sections is applied to the electromagnetic configuration shown in Fig. 1 to analyze the convergence of the solutions. The dimensions and parameters of the model are given in Fig. 3 and Table I. The convergence is analyzed at frequencies of 100 Hz and 10 kHz. At 10 kHz and the specified conductivity, the skin depth is approximately 1 mm. Both the force and power loss are calculated as a function of the number of harmonics used in the x- and y-direction for the two frequencies and are depicted in Fig. 4 and Fig. 5. The available memory allows to calculate results up to a maximum number of harmonics equal to $N = M = 70$.

In Fig. 4 and Fig. 5, for each number of harmonics pair, the relative error with respect to the result with the maximum number of harmonics ($N = M = 70$) is calculated. It can be seen that the solution for F_z converges to an error of less than 3% (w.r.t the result for $N = M = 70$) when $N > 30$ and $M > 40$, for both frequencies. As regards the power loss calculation at

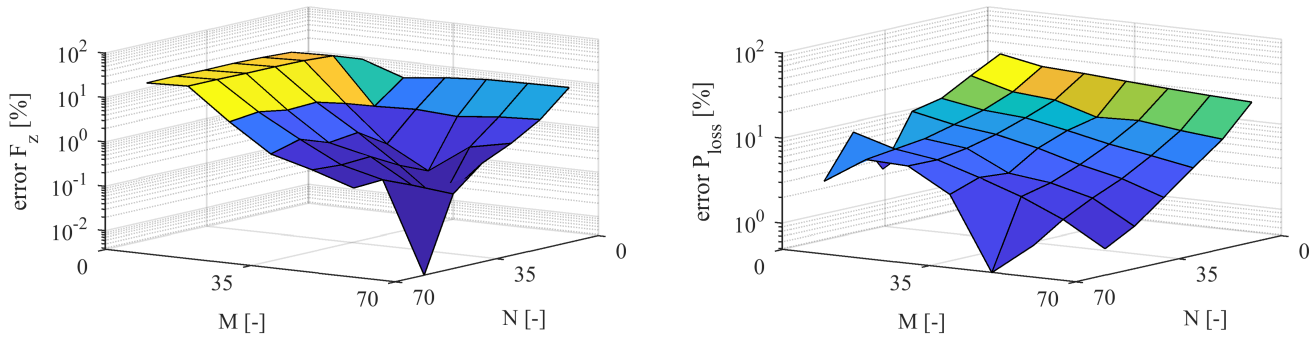

(a) (b)

Fig. 5. Convergence plots as a function of the number of harmonics at a frequency of 10 kHz. The relative error with respect to the result at $N = M = 70$ is calculated for each harmonic pair: a) convergence of the force in the z-direction, b) convergence of the power loss (in both conducting segments).

TABLE II
ERRORS IN FIG. 7 ACCORDING TO (62)

Freq.	cp_{xy1}	cp_{xy2}	cp_{xz1}	cp_{xz2}	cp_{yz1}	cp_{yz2}
100 Hz	13.7%	14.0%	13.3%	7.5%	9.8%	9.9%
10 kHz	21.4%	21.1%	21.4%	18.9%	22.9%	19.9%

100 Hz, an error less than 3% is obtained when $M > 50$ and $N > 40$. The convergence of the power loss calculation at 10 kHz is more unstable and becomes less than 3% when $M > 60$ and $N > 60$. It is concluded that the power loss calculation needs more harmonics than the force calculation to obtain an accurate result. This is due to the fact that the power loss calculation relies heavily on the current distribution in the plate. As will be shown in the next section, especially for higher frequencies, all current is flowing in the edges of the plates. To model this accurately, a high spatial resolution is necessary and, therefore, a relatively large number of harmonics in both directions is required.

B. Model validation

To verify the obtained results, they are compared to results obtained with finite element method (FEM) software Flux 3D (Ced, 2015). In the FEM software, the geometry of Fig. 1 is implemented and a mesh is applied. At the top of the airgap and the bottom of the conducting plates a meshsize of 0.2 mm is applied. In the other parts of the airgap and plates, the mesh size varies from 0.2 to 1 mm. The number of second-order volume mesh-elements is equal to 1087208 in the FEM model. The approximating functions for vector potential formulations is set to edge finite elements. The applied boundary conditions and periodicity are the same as in the semi-analytical model.

For the highest frequency analyzed (10 kHz), the magnetic flux density in the center of the air gap (on a xy-plane) between the coil and the conducting segments is calculated via harmonic modeling and compared to FEM. To calculate the field in the airgap, the number of harmonics taken into account is equal to N = 30, M = 40. The results are shown in Fig. 6. A relative error with respect to the results obtained with 3D FEM is computed through

$$\frac{\text{rms}(|\vec{B}_{ANA} - \vec{B}_{FEM}|)}{\text{rms}(|\vec{B}_{FEM}|)} \times 100\%, \tag{62}$$

where rms is the root mean square of the error. The relative error with respect to FEM in Fig. 6 is equal to 4.0%.

The current density inside the conducting plates is obtained on several cut-planes, which are shown in Fig. 3. To calculate the current density distribution, the maximum number of harmonics is used, so N = 70 and M = 70. In Fig. 7, the magnitude of the current density in the cut-planes for two frequencies (100 Hz and 10 kHz) is depicted. For the frequency of 10 kHz the currents are flowing mainly at the bottom and edges of the plate. In Table II the relative error with respect to the FEM, calculated according to (62), has been listed for each cut-plane. In Fig. 7, it can be seen that the largest errors in the current density distribution are located at the edges of the plate, where, especially for higher frequencies, most of the current is flowing. Due to the Gibbs effect in the description of the spatially dependent conductivity, the discrepancy between the developed method and FEM is increased in the edges of the plate.

The developed model is verified by analyzing the force and power loss over a range of frequencies (up to 10 kHz). To obtain the force, N and M were set to 30 and 40, respectively, because in the preceding section it was shown that the error

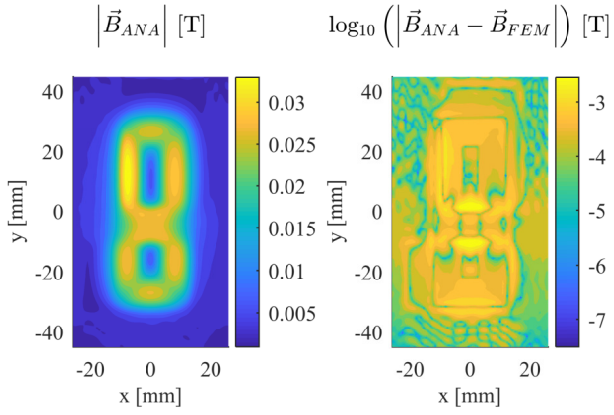

Fig. 6. Absolute value of the magnetic flux density on the xy-plane at z = 8.5 mm. The result obtained with the semi-analytical model (ANA) is shown on the left side. On the right, the difference with the FEM result is depicted.

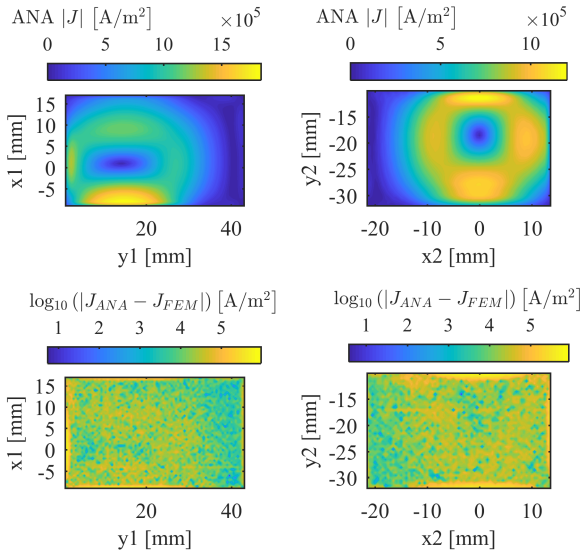

a. Results on the cut planes cp_{xy1} and cp_{xy2} for $f = 100$ Hz.

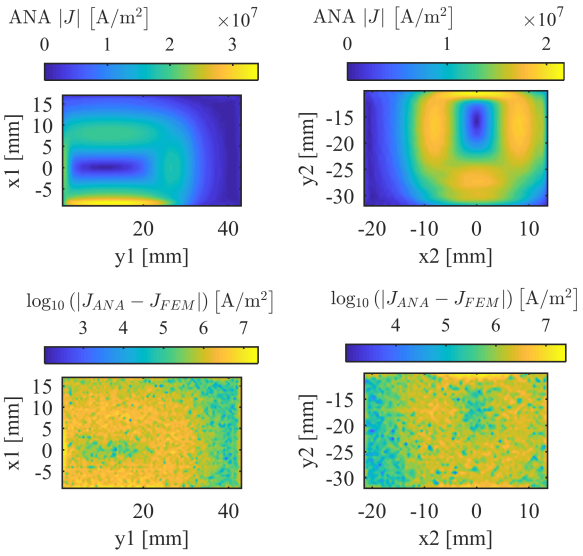

b. Results on the cut planes cp_{xy1} and cp_{xy2} for $f = 10$ kHz.

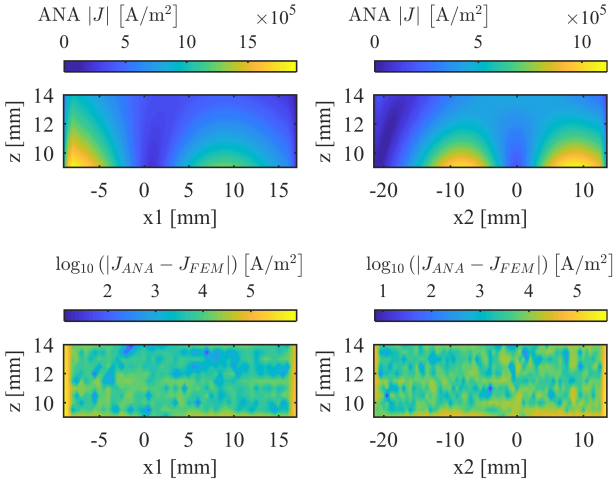

c. Results on the cut planes cp_{xz1} and cp_{xz2} for $f = 100$ Hz.

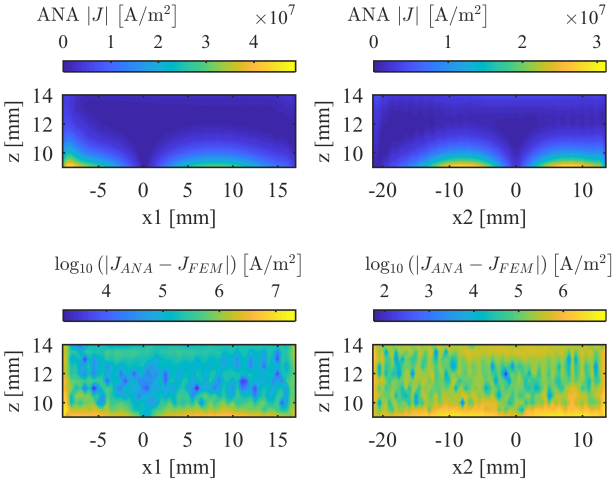

d. Results on the cut planes cp_{xz1} and cp_{xz2} for $f = 10$ kHz.

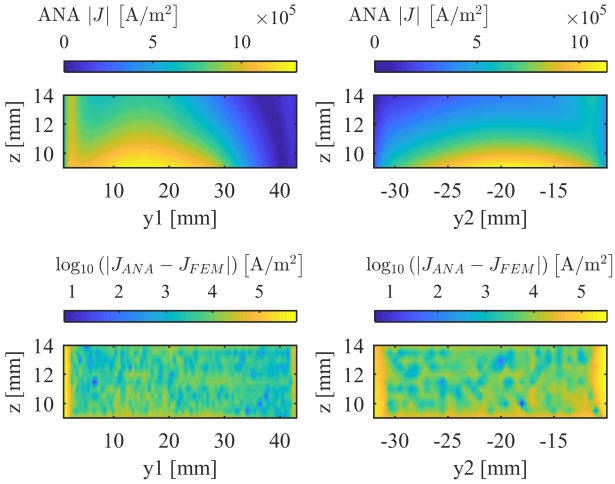

e. Results on the cut planes cp_{yz1} and cp_{yz2} for $f = 100$ Hz.

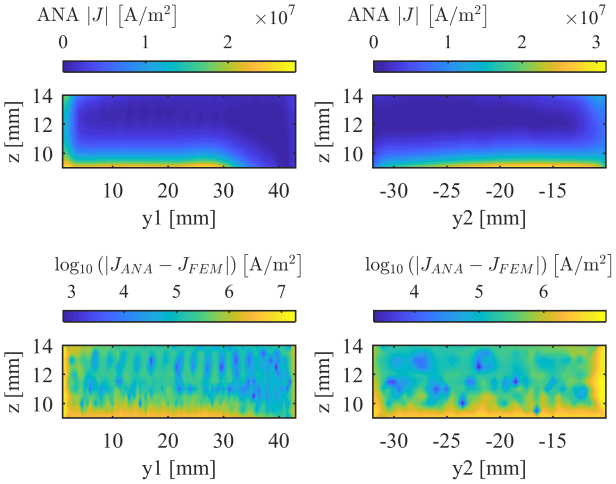

f. Results on the cut planes cp_{yz1} and cp_{yz2} for $f = 10$ kHz.

Fig. 7. Obtained magnitude of the current density via the analytical (ANA) model (top figures) and the log10 of the absolute error with respect to FEM (bottom figures).

between results, when the number of harmonics is increased, is less than 5%. The comparison of the calculated forces with the FEM results is depicted in Fig. 8a. The relative error in the force compared to FEM, in the x- and z-direction is less than 5% for frequencies above 100 Hz, where the force is larger than 0.5 mN. The error in the force in the y-direction is at 60 % maximum, because the force is close to zero over the full frequency range. Also the power loss over a range of frequencies is analyzed and is shown in Fig. 8b. To calculate the results with the semi-analytical model, the maximum number of harmonics is used in both directions (N = 70 and M = 70), because the power loss calculation shows a relatively slow convergence at high frequencies. The relative error with respect to the FEM is 13.5% at 10 kHz and below 7.5% for frequencies below 1 kHz.

Using the hardware available (quadcore Intel Core i7-4790 with 32GB RAM), the computation times of semi-analytical methods is depicted as a function of the number of considered harmonics in Fig. 9. As a reference, also the computation time of FEM for the 10 kHz mesh is given in the figure. The computation times shown, concern the total amount of time needed to calculate the force and power loss results. Up till a total number of 3600 considered harmonic pairs, the developed method computes the results faster than FEM. The mesh generation and solving time for FEM depend on the implemented mesh and can be optimized, regarding the problem at hand. Also for the semi-analytical model, code optimization and implementation could improve the computation time. Therefore, it can be concluded, that for a relatively low number of harmonics (e.g. 41 $\times$ 41 harmonics) the semi-analytical model is significantly faster than 3D FEM.

VIII. Conclusion

A 3D semi-analytical harmonic modeling technique has been described to calculate electromagnetic field quantities in segmented electrically conducting regions of a periodic model. The spatially varying conductivity of a segmented conducting region has been included in the solution of magnetic field and induced current density components, in the Cartesian coordinate system. The method can be further developed to model eddy currents in other coordinate systems. Incorporation of the conductivity is made possible by a field formulation using the tangential components of the electric and magnetic field. In the non-conducting regions, the classical 3D harmonic model formulations has been applied. Because solutions for different types of regions and their coupling have been described, eddy current effects in almost any electromagnetic configuration, consisting of coils, magnets or conducting material can be analyzed by proper selection and composition of the region types. Segmentation or slit patterns in conducting materials can be described by the double Fourier series, resulting from analytical expressions or the Fast-Fourier transform. In conclusion, a wide range of conducting structures can be modeled and a flexible method has been developed. The semi-analytical technique has been applied to a topology containing a coil and two pieces of conducting material. The force calculation shows relatively fast convergence, while the convergence of the power loss calculation requires a higher number of harmonics. The results on force and power loss have been compared to results obtained with FEM for a range of frequencies (up to 10 kHz). The force components calculations show good agreement with FEM results. The power loss calculations give a error of 13.5% at 10 kHz, but below 7.5% for frequencies below 1 kHz. It can be concluded that an accurate semi-analytical method to calculate eddy currents in 3D segmented structures has been developed. For a relatively low number of harmonics, the method is a fast and more memory efficient alternative to the finite element method.

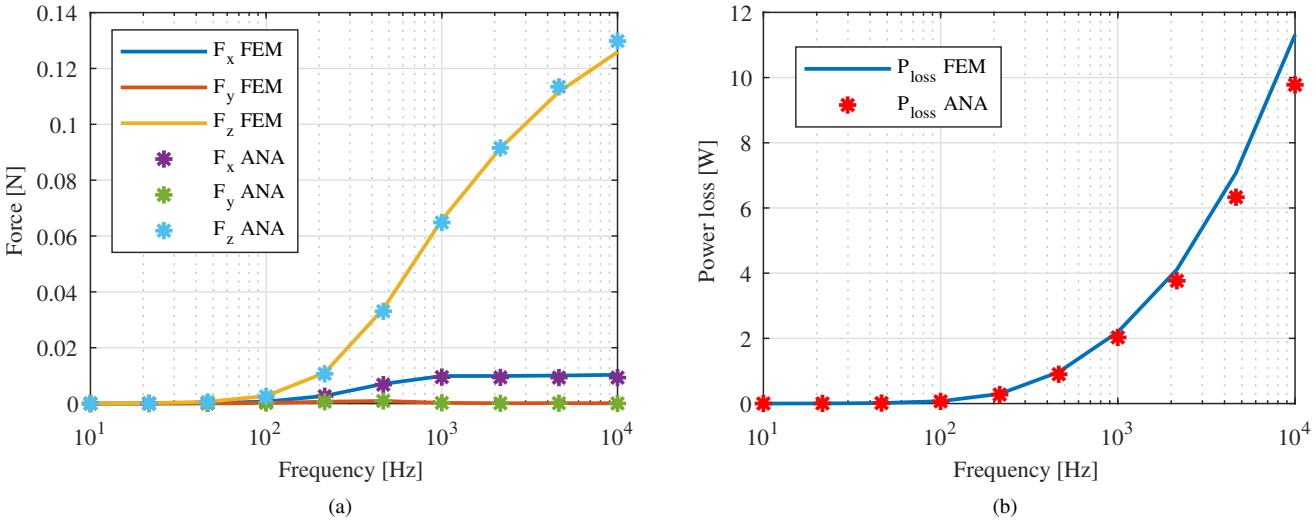

Fig. 8. a) Force components calculated with the developed semi-analytical (ANA) model and FEM. b) Power loss calculated with the developed semi-analytical (ANA) model and FEM.

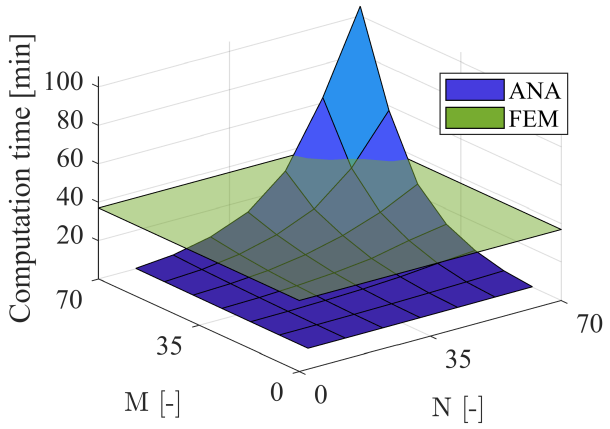

Fig. 9. Computation times of the compared methods.

APPENDIX
SOLUTIONS IN NON-CONDUCTING REGIONS

For regions with the magnetic scalar potential formulation, such as air regions or a region containing magnets, the solutions for the magnetic field strength components, following from (4) and (12), are

$$\mathbf{h_x} = \mathbf{K_x}\ \mathbf{\Lambda}\left(\mathbf{\Theta}^{+}(\boldsymbol{\lambda}, z)\ \mathbf{c}^{+} - \mathbf{\Theta}^{-}(\boldsymbol{\lambda}, z)\ \mathbf{c}^{-} + \mathbf{p}_{\psi}\right), \tag{63}$$

$$\mathbf{h_y} = \mathbf{K_y}\ \mathbf{\Lambda}\left(\mathbf{\Theta}^{+}(\boldsymbol{\lambda}, z)\ \mathbf{c}^{+} - \mathbf{\Theta}^{-}(\boldsymbol{\lambda}, z)\ \mathbf{c}^{-} + \mathbf{p}_{\psi}\right), \tag{64}$$

$$\mathbf{h_z} = -j\mathbf{\Lambda}^2\left(\mathbf{\Theta}^{+}(\boldsymbol{\lambda}, z)\ \mathbf{c}^{+} + \mathbf{\Theta}^{-}(\boldsymbol{\lambda}, z)\ \mathbf{c}^{-}\right), \tag{65}$$

where

$$\boldsymbol{\lambda} = \sqrt{\mathbf{k_x}^2 + \mathbf{k_y}^2}. \tag{66}$$

The solutions for the magnetic flux density components are, from (5), equal to

$$\mathbf{b_x} = \mu_0\mu_r\mathbf{h_x} + \mu_0\mathbf{m_x}, \tag{67}$$

$$\mathbf{b_y} = \mu_0\mu_r\mathbf{h_y} + \mu_0\mathbf{m_y}, \tag{68}$$

$$\mathbf{b_z} = \mu_0\mu_r\mathbf{h_z} + \mu_0\mathbf{m_z}. \tag{69}$$

For regions with the vector potential formulation, such as regions containing a current carrying coil, the solutions are given by

$$\mathbf{h_x} = \mathbf{K_x}\ \mathbf{\Lambda}\left(\mathbf{\Theta}^{+}(\boldsymbol{\lambda}, z)\ \mathbf{c}^{+} - \mathbf{\Theta}^{-}(\boldsymbol{\lambda}, z)\ \mathbf{c}^{-} + \mathbf{p}_{\psi}\right), \tag{70}$$

$$\mathbf{h_y} = \mathbf{K_y}\ \mathbf{\Lambda}\left(\mathbf{\Theta}^{+}(\boldsymbol{\lambda}, z)\ \mathbf{c}^{+} - \mathbf{\Theta}^{-}(\boldsymbol{\lambda}, z)\ \mathbf{c}^{-} + \mathbf{p}_{\psi}\right), \tag{71}$$

$$\mathbf{h_z} = -j\mathbf{\Lambda}^2\left(\mathbf{\Theta}^{+}(\boldsymbol{\lambda}, z)\ \mathbf{c}^{+} + \mathbf{\Theta}^{-}(\boldsymbol{\lambda}, z)\ \mathbf{c}^{-}\right) + j\mathbf{K_x}\mathbf{p}_{a_y} - j\mathbf{K_y}\mathbf{p}_{a_x}, \tag{72}$$

where

$$\boldsymbol{\lambda} = \sqrt{\mathbf{k_x}^2 + \mathbf{k_y}^2}. \tag{73}$$

The scalar potential used in the boundary conditions (for a vector potential region), derived from H_x and H_y using (49), is equal to

$$\boldsymbol{\psi} = j\mathbf{\Lambda}\left(\mathbf{\Theta}^{+}(\boldsymbol{\lambda}, z)\ \mathbf{c}^{+} - \mathbf{\Theta}^{-}(\boldsymbol{\lambda}, z)\ \mathbf{c}^{-}\right). \tag{74}$$

REFERENCES

Benlamine, R., Dubas, F., Randi, S. A., Lhotellier, D. and Espanet, C. (2015), "3-D numerical hybrid method for PM eddy-current losses calculation: Application to axial-flux pmsms", *IEEE Transactions on Magnetics*, Vol. 51 No.7 , pp. 1–10.

Biro, O. and Preis, K. (1989), "On the use of the magnetic vector potential in the finite-element analysis of three-dimensional eddy currents", *IEEE Transactions on Magnetics*, Vol. 25 No.4 , pp. 3145–3159.

Bossavit, A. (1988), "A rationale for 'edge-elements' in 3-D fields computations", *IEEE Transactions on Magnetics*, Vol. 24 No.1 , pp. 74–79.

Ced (2015), *Flux 12 User's guide*, release 12.0 edn.

Custers, C. H. H. M., Jansen, J. W. and Lomonova, E. A. (2017*a*), "2-d semi-analytical modeling of eddy currents in multiple non-connected conducting elements", *IEEE Transactions on Magnetics*, Vol. 53 No.11 , pp. 1–6.

Custers, C. H. H. M., Jansen, J. W. and Lomonova, E. A. (2017*b*), Modeling and experimental validation of field distributions due to eddy currents in slitted conducting plates, *in* '2017 11th International Symposium on Linear Drives for Industry Applications (LDIA)', pp. 1–6.

Custers, C. H. H. M., Jansen, J. W., van Beurden, M. C. and Lomonova, E. A. (2016), 3D harmonic modeling of magnetostatic fields including rectangular structures with finite permeability, *in* '2016 XXII International Conference on Electrical Machines (ICEM)', pp. 1230–1236.

Custers, C. H. H. M., Overboom, T. T., Jansen, J. W. and Lomonova, E. A. (2015), "2-D semi-analytical modeling of eddy currents in segmented structures", *IEEE Transactions on Magnetics*, Vol. 51 No.11 , pp. 1–4.

Dwivedi, A., Singh, S. K. and Srivastava, R. K. (2016), "Analysis of permanent magnet brushless ac motor using Fourier transform approach", *IET Electric Power Applications*, Vol. 10 No.6 , pp. 539–547.

Ede, J. D., Atallah, K., Jewell, G. W., Wang, J. B. and Howe, D. (2007), "Effect of axial segmentation of permanent magnets on rotor loss in modular permanent-magnet brushless machines", *IEEE Transactions on Industry Applications*, Vol. 43 No.5 , pp. 1207–1213.

Fireteanu, V., Paya, B., Nuns, J. and Tudorache, T. (2002), "Eddy currents in thin plates modelled as surface regions", *COMPEL - The international journal for computation and mathematics in electrical and electronic engineering*, Vol. 21 No.4 , pp. 581–590.

Furlani, E. (2001), *Permanent Magnet and Electromechanical Devices*, Academic Press.

Hamming, R. W. (1986), *Numerical Methods for Scientists and Engineers (2nd edition)*, Dover Publications, Inc., New York, NY, USA.

Hannon, B., Sergeant, P. and Dupré, L. (2017), "Study of the effect of a shielding cylinder on the torque in a permanent-magnet synchronous machine considering two torque-producing mechanisms", *IEEE Transactions on Magnetics*, Vol. 53 No.10 , pp. 1–8.

Jansen, J. W., Smeets, J. P. C., Overboom, T. T., Rovers, J. M. M. and Lomonova, E. A. (2014), "Overview of analytical models for the design of linear and planar motors", *IEEE Transactions on Magnetics*, Vol. 50 No.11 , pp. 1–7.

Jayaraman, S., Esakkirajan, S. and Veerakumar, T. (2011), *Digital Image Processing*, McGraw-Hill Education (India) Pvt Limited.

Jumayev, S., Paulides, J. J. H., Boynov, K. O., Pyrhönen, J. and Lomonova, E. A. (2016), "3-D analytical model of helical winding pm machines including rotor eddy currents", *IEEE Transactions on Magnetics*, Vol. 52 No.5 , pp. 1–8.

Kim, H., Song, C., Kim, D. H., Jung, D. H., Kim, I. M., Kim, Y. I., Kim, J., Ahn, S. and Kim, J. (2016), "Coil design and measurements of automotive magnetic resonant wireless charging system for high-efficiency and low magnetic field leakage", *IEEE Transactions on Microwave Theory and Techniques*, Vol. 64 No.2 , pp. 383–400.

Kim, H., Song, C., Kim, D. H. and Kim, J. (2015), Design of conductive shield for wireless power transfer system for electric vehicle considering automotive body, *in* '2015 IEEE International Symposium on Electromagnetic Compatibility (EMC)', pp. 1369–1374.

Lee, S. Y., Woo, D. K., Ro, J. S. and Jung, H. K. (2013), "Analysis of a permanent magnet machine for a high power density taking losses into consideration", *IEEE Transactions on Magnetics*, Vol. 49 No.5 , pp. 1765–1768.

Meessen, K. J., Paulides, J. J. H. and Lomonova, E. A. (2012), "Modeling of magnetization patterns for 2 dof rotary linear actuators", *COMPEL - The international journal for computation and mathematics in electrical and electronic engineering*, Vol. 31 No.5 , pp. 1428–1440.

Mirzaei, M., Binder, A. and Deak, C. (2010), 3D analysis of circumferential and axial segmentation effect on magnet eddy current losses in permanent magnet synchronous machines with concentrated windings, *in* 'The XIX International Conference on Electrical Machines - ICEM 2010', pp. 1–6.

Nair, S. S., Wang, J., Chin, R., Chen, L. and Sun, T. (2017), "Analytical prediction of 3-d magnet eddy current losses in surface mounted pm machines accounting slotting effect", *IEEE Transactions on Energy Conversion*, Vol. 32 No.2 , pp. 414–423.

Nakano, T., Kawase, Y., Yamaguchi, T., Nakamura, M. and Nishikawa, N. (2013), "3-D finite element analysis of eddy current in laminated cores of the interior permanent-magnet motor", *IEEE Transactions on Magnetics*, Vol. 49 No.5 , pp. 1945–1948.

Paul, S. and Bird, J. Z. (2013), "A 3-d analytic eddy current model for a finite width conductive plate", *COMPEL - The international journal for computation and mathematics in electrical and electronic engineering*, Vol. 33 No.1/2 , pp. 688–706.

Pluk, K. J. W., Jansen, J. W. and Lomonova, E. A. (2015), "Modeling of noncuboidal magnetic sources in 3-D Fourier modeling", *IEEE Transactions on Magnetics*, Vol. 51 No.11 , pp. 1–4.

Rovers, J. M. M., Jansen, J. W. and Lomonova, E. A. (2011), "Disturbance effects of electrically conductive material in the air gap of a linear permanent magnet synchronous motor", *IEEE Transactions on Magnetics*, Vol. 47 No.10 , pp. 2668–2671.

Shah, M. R. and Lee, S. B. (2006), "Rapid analytical optimization of eddy-current shield thickness for associated loss minimization in electrical machines", *IEEE Transactions on Industry Applications*, Vol. 42 No.3 , pp. 642–649.

Smeets, J. P. C., Overboom, T. T., Jansen, J. W. and Lomonova, E. A. (2013), "Three-dimensional analytical modeling

technique of electromagnetic fields of air-cored coils surrounded by different ferromagnetic boundaries", *IEEE Transactions on Magnetics*, Vol. 49 No.12 , pp. 5698–5708.

Takahashi, N., Shinagawa, H., Miyagi, D., Doi, Y. and Miyata, K. (2009), "Analysis of eddy current losses of segmented Nd-Fe-B sintered magnets considering contact resistance", *IEEE Transactions on Magnetics*, Vol. 45 No.3 , pp. 1234–1237.

Theodoulidis, T., Antonopoulos, C. and Kriezis, E. (1995), "Analytical solution for the eddy current problem inside a conducting cylinder using the second order magnetic vector potential", *COMPEL - The international journal for computation and mathematics in electrical and electronic engineering*, Vol. 14 No.4 , pp. 45–48.

Wu, L. J., Zhu, Z. Q., Staton, D., Popescu, M. and Hawkins, D. (2012), "Analytical model for predicting magnet loss of surface-mounted permanent magnet machines accounting for slotting effect and load", *IEEE Transactions on Magnetics*, Vol. 48 No.1 , pp. 107–117.

Xiao, C., Wei, K., Cheng, D. and Liu, Y. (2017), "Wireless charging system considering eddy current in cardiac pacemaker shell: Theoretical modeling, experiments, and safety simulations", *IEEE Transactions on Industrial Electronics*, Vol. 64 No.5 , pp. 3978–3988.

Yamazaki, K. and Abe, A. (2009), "Loss investigation of interior permanent-magnet motors considering carrier harmonics and magnet eddy currents", *IEEE Transactions on Industry Applications*, Vol. 45 No.2 , pp. 659–665.

Zhu, H., Teo, T. J. and Pang, C. K. (2015), Analysis of force harmonics and eddy current damping for 2 dof moving magnet linear motor, *in* 'IECON 2015 - 41st Annual Conference of the IEEE Industrial Electronics Society'.